Integrative Biology, 2021, 13(1),1–16

doi: 10.1093/intbio/zyaa024
Advance Access publication January 14, 2021
Original Article

ORIGINAL ARTICLE

Growth of tumor emboli within a vessel model reveals dependence on the magnitude of mechanical constraint

Jonathan Kulwatno[1,2], Jamie Gearhart[2,3], Xiangyu Gong[2,3], Nora Herzog[2,3], Matthew Getzin[1,2], Mihaela Skobe[4], and Kristen L. Mills[2,3,*]

[1]Department of Biomedical Engineering, Rensselaer Polytechnic Institute, Troy, NY, USA, [2]Center for Biotechnology and Interdisciplinary Studies, Rensselaer Polytechnic Institute, Troy, NY, USA, [3]Department of Mechanical, Aerospace, and Nuclear Engineering, Rensselaer Polytechnic Institute, Troy, NY, USA, and [4]Department of Oncological Sciences & Tisch Cancer Institute, Icahn School of Medicine at Mount Sinai, New York, NY, USA

*Corresponding author. E-mail: MillsK2@RPI.edu

Abstract

Tumor emboli—aggregates of tumor cells within vessels—pose a clinical challenge as they are associated with increased metastasis and tumor recurrence. When growing within a vessel, tumor emboli are subject to a unique mechanical constraint provided by the tubular geometry of the vessel. Current models of tumor emboli use unconstrained multicellular tumor spheroids, which neglect this mechanical interplay. Here, we modeled a lymphatic vessel as a 200 μm-diameter channel in either a stiff or soft, bioinert agarose matrix to create a vessel-like constraint model (VLCM), and we modeled colon or breast cancer tumor emboli with aggregates of HCT116 or SUM149PT cells, respectively. The stiff matrix VLCM constrained the tumor emboli to the cylindrical channel, which led to continuous growth of the emboli, in contrast to the growth rate reduction that unconstrained spheroids exhibit. Emboli morphology in the soft matrix VLCM, however, was dependent on the magnitude of mechanical mismatch between the matrix and the cell aggregates. In general, when the elastic modulus of the matrix of the VLCM was greater than the emboli ($E_{VLCM}/E_{emb} > 1$), the emboli were constrained to grow within the channel, and when the elastic modulus of the matrix was less than the emboli ($0 < E_{VLCM}/E_{emb} < 1$), the emboli bulged into the matrix. Due to a large difference in myosin II expression between the cell lines, we hypothesized that tumor cell aggregate stiffness is an indicator of cellular force-generating capability. Inhibitors of myosin-related force generation decreased the elastic modulus and/or increased the stress relaxation of the tumor cell aggregates, effectively increasing the mechanical mismatch. The increased mechanical mismatch after drug treatment was correlated with increased confinement of tumor emboli growth along the channel, which may translate to increased tumor burden due to the increased tumor volume within the diffusion distance of nutrients and oxygen.

Key words: tumor; microchannel; tumor emboli; metastasis; force generation

Received May 19, 2020; **revised** September 2, 2020; **accepted** December 3, 2020

INSIGHT BOX

The growth of tumor emboli—aggregates of tumor cells within vessels—is associated with aggressive cancer progression and metastasis. Models of their growth have not taken into account their biomechanical context, where radial expansion is constrained, but lengthwise expansion is free in the vessel. Here, we modeled lymphatic vessel geometry with a cylindrical microchannel in a hydrogel. In contrast to unconstrained or fully embedded aggregates, our VLCM promotes the growth of emboli. The growth advantage is increased when the matrix is stiffened or actomyosin contractility weakened, both of which effectively increase the magnitude of mechanical constraint. This study sheds light on increased tumor burden in vessel-based growth and indicates a need to study tumor progression in similar environments.

INTRODUCTION

As part of the metastatic cascade for many human solid cancers, it has been estimated that 80% of cases involve tumor cells invading the lymphatic system [1] either individually or as cohesive groups [2]. Tumor cells are then often carried via lymphatic vessels to regional lymph nodes, evidenced by their use as a reliable predictor of the extent of metastatic spread [3]. However, they can also arrest as cohesive groups, known as tumor emboli, and grow within lymphatic vessels [2, 4, 5] (Fig. 1). Lymphatic tumor emboli occur in several cancer types, notably melanoma [6], breast [7], esophageal [8] and colorectal cancer [9, 10], and, in some instances, form at a rate greater than local lymph node metastases [8]. A particularly extreme case of tumor growth within lymphatic vessels is associated with inflammatory breast cancer (IBC). In this most aggressive type of breast cancer with a high potential for metastasis and mortality, IBC cells invade and extensively spread through the dermal lymphatic vessels [11, 12]. The presence of tumor emboli in the lymphatic vasculature, with or without lymph node involvement, is associated with increased metastasis [8, 13] and has been correlated with poor patient prognosis [7, 9, 10, 14]. Despite their importance for metastatic spread, little is understood about what factors influence the growth of tumor emboli [10, 13, 15, 16].

Inside the lymphatic vessel, tumor cells and tumor emboli can have a number of interactions with the environment including lymph fluid flow, chemokine signaling and adhesive interactions with lymphatic endothelial cells [17]. Once the tumor embolus grows to block, or occlude, the vessel, however, it will exert force upon the surrounding extracellular matrix. This is an important biomechanical interaction—the effects of which have not been investigated on the growth of tumor emboli. Appropriate *in vitro* models of the specific environment of tumor emboli, taking into consideration factors such as geometry and matrix mechanical properties, are necessary to study such interactions.

Currently, the progression of tumor emboli is primarily studied *in vitro* using multicellular tumor spheroids (MCTSs) [15, 18, 19]. Most MCTS models derive from the aggregation of tumor cells on non-adhesive surfaces. MCTSs are three-dimensional structures that better recapitulate *in vivo* tumors in form and behavioral responses than 2D Petri dish culture [20–22]. However, they only account for tumor cell-tumor cell interactions and neglect interactions with their microenvironments. Solid tumors grow under mechanical constraints provided by their surrounding tissue [23–25]. As such, there is an interplay between a tumor and its microenvironment due to the competition for space: a growing tumor expands against the surrounding tissue while the surrounding tissue confines the tumor. Experimentalists have isolated this biomechanical crosstalk by fully embedding tumor cells within tissue-mechanics-mimicking hydrogels, which has

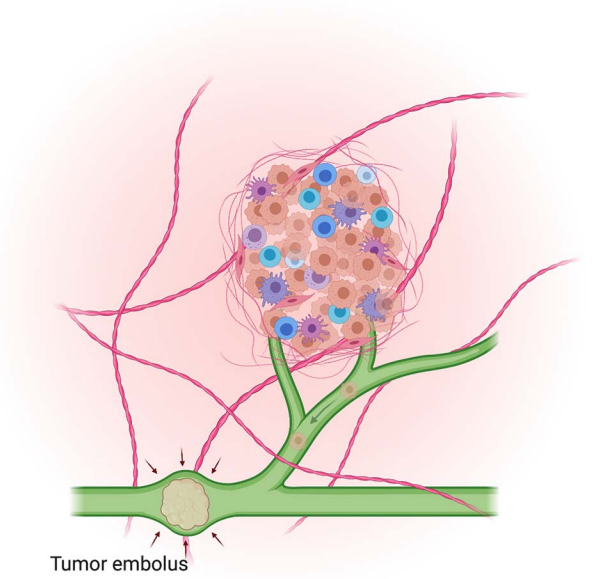

Figure 1. Schematic of a tumor embolus arrested and growing within a lymphatic vessel. The resistance to radial growth against the vessel wall depends on the mechanical properties (e.g. stiffness) of the extracellular matrix surrounding it. Created with BioRender.com.

provided insights into how growth and disease progression are influenced by the compressive stress provided by the microenvironment [23–30]. Compressive stress has been shown to inhibit the growth of tumor cells and tumor cell aggregates by affecting proliferation and apoptosis, but also stimulating the migration of carcinoma cells [24–26, 29].

Studies of compressive stress on tumors have focused mainly on uniform stresses acting on solid tumors, assuming that the solid tumor is confined within the connective tissue. However, in the context of tumor emboli, the tumor is only constrained by the geometry of the vessel, which can be simplified as a cylindrical channel. Here, a growing tumor embolus freely expands until it reaches the boundaries of the vessel, at which point continued expansion is constrained only at the circumference of the vessel to a degree proportional to the stiffness of the surrounding tissue. Therefore, the model microenvironment of tumor emboli—a vessel-like constraint model (VLCM)—lies between that of no constraint, as the MCTS models, and fully embedding tumor cells or tumor cell aggregates within a hydrogel matrix. Recently, the growth of tumor cell aggregates and the pressure they exert in tubular hydrogel capsules was measured and a mathematical

model was used to investigate the effects of the constraint and oxygen on the dynamics of growth [31]. The mathematical model of Le Maout *et al*. [31] investigated the dynamics of the aggregate growth assuming a rigid-walled channel and found that both the pressure built up in the aggregate and oxygen depletion affected the growth dynamics.

In this study, we aimed to gain insights into how biomechanical interactions between tumor emboli and the surrounding matrix influence the growth of the tumor emboli within the lymphatic vasculature. Our VLCM consisted of a cylindrical microchannel formed within a matrix of tissue-mechanics-mimicking hydrogel. We compared the growth and morphology of unconstrained MCTSs to those constrained in our VLCM. Changing the mechanical properties of the VLCM matrix modified the growth and morphology of model tumor emboli from two cell lines: human colon cancer cells (HCT116) and human IBC cells (SUM149PT) that represent cells derived from cancers where tumor emboli are frequently observed [10, 32, 33]. Further, the growth behavior—whether the tumor emboli were confined to the VLCM channel or bulged into the matrix—was determined by the mismatch in the mechanical properties between the hydrogel matrix and tumor cell aggregates, which was modulated by inhibition of myosin-related force-generating mechanisms.

MATERIALS & METHODS

Cell culture

HCT116 human colon cancer cells were purchased from ATCC. Cells were grown as monolayers in McCoy's 5A medium (Sigma) supplemented with 10% FBS (Gibco) and ×1 antimycotic/antibiotic solution (Gibco) in an incubator at 37°C and 5% CO_2. Upon reaching 80–90% confluency, cells were collected using 0.05% trypsin (Gibco), centrifuged to remove the collection media and replaced with fresh media.

SUM149PT human IBC cells were generously provided by Dr. Jason Herschkowitz of the University at Albany. Cells were grown as monolayers in Ham's F-12 medium (Biowhitaker) supplemented with 5% FBS (Gibco), ×1 antimycotic/antibiotic solution (Gibco), 5 µg/ml insulin (Gibco) and 1 µg/ml hydrocortisone (Acros) in an incubator at 37°C and 5% CO_2. Upon reaching 80–90% confluency, cells were collected using 0.05% trypsin (Gibco), centrifuged to remove the collection media and replaced with fresh media.

Tumor spheroid generation and growth

In a 96-well plate, 50 µl of molten 1.0% agarose was pipetted into each well and placed at 4°C for 30 min to gel. After gelation, 200 µl of the respective media for each cell line was pipetted into the wells. Cells were then seeded at 1000 cells per well and centrifuged for 10 min at 200 × g. The spheroids were cultured in an incubator at 37°C and 5% CO_2 for 20 days for growth studies, 10 days for mechanical testing and drug inhibition experiments, and 7 days for western blotting. Media was not changed during the growth period. Brightfield images of the tumor spheroids were taken daily using an Axio Vert.A1 (Zeiss).

Template for molding cylindrical channels in hydrogels

Three-dimensional printed templates were used to aid in the fabrication of cylindrical channels in agarose hydrogels. The templates were printed with acrylonitrile butadiene styrene using a UPrint SE Plus (Stratasys). The templates consisted of a walled rectangular opening with inlets on opposite ends to accommodate a trimmed needle guide on either end. A commercially available, solid stainless-steel rod—200 µm diameter (Seirin)—was threaded through the two needles to span the rectangular opening of the template (Fig. 2A). Polydimethylsiloxane (PDMS) was poured into two large U-shaped pockets wrapped around either side of the rectangular opening and cured. A trimmed microscope slide (Globe Scientific) was placed below the template and secured by binder clips that bonded the slide to the PDMS, ensuring a seal between the glass and the template. All components were either soaked in 70% ethanol overnight or kept under UV for sterilization prior to assembly. The needles were coated with sterile silicone oil during assembly to decrease agarose adhesion.

The suspended 200-µm-diameter rod was used as a template to mold cylindrical channels in agarose hydrogels (Sigma, low-gelling temperature). Two different agarose concentrations were used: 0.3% (w/v) to provide a soft matrix and 1.0% (w/v) to provide a stiff matrix. In either case, agarose powder was dissolved in PBS at 100°C then cooled to 40°C before use. The templates were pre-cooled at 4°C for 10 min prior to the addition of molten agarose, which was pipetted into the rectangular opening of assembled templates. The agarose was allowed to cool at 4°C for 20 min, after which the solid rod and the needles were carefully removed. To confirm the integrity of the microchannel, fluorescent microbeads of 200 nm (ThermoFisher) were mixed in an 0.3% agarose solution at a concentration of 5.30×10^9 beads/ml before gelation and then imaged (Fig. 2B).

Two different templates were produced that differed in the dimension of the rectangular opening in order to accommodate higher aspect ratio growth of tumor cell aggregates in channels in the stiff agarose. In particular, the shorter template had inner dimensions of 15 mm (length) × 10 mm (width) × 2.25 mm (depth), which held 450 µl of soft, 0.3% (w/v), agarose. The inlets on opposite ends of the rectangular opening were 0.908 mm in diameter (Fig. 2A) through which two 20-gauge needles (20G, O.D. = 0.908 mm; B.D.) were inserted. The longer template had inner dimensions of 30 mm (length) × 8.5 mm (width) × 1.75 mm (depth) (Supplementary Figure S1), which held 750 µl of the stiff, 1.0% (w/v) agarose. The inlets on opposite ends of the rectangular opening were 0.819 mm in diameter (Supplementary Figure S1) through which a normal and a trimmed 21-gauge needle (21G, O.D. = 0.819 mm; B.D.) were inserted.

Tumor emboli generation and growth

A cell suspension containing either HCT116 cells at 1×10^5 cells/ml or SUM149PT cells at 3×10^5 cells/ml was injected with a pipette into the channel through the inlets. Flow-through of the now-hollow microchannel was aided by brief and shallow tilting of the template. The microchannel-containing hydrogels were then gently transferred out of the templates and into Petri dishes and incubated while the cells were allowed to form aggregates within the microchannels. Once the aggregates reached the diameter of the microchannel, which took between 5 and 7 days, they were deemed emboli. Emboli-containing samples were cultured in clean Petri dishes (to eliminate the cells that had leaked out of the channel and attached to the dish), with fresh culture media, in an incubator for 20 days for growth studies or 10 days for drug inhibition experiments. Media was

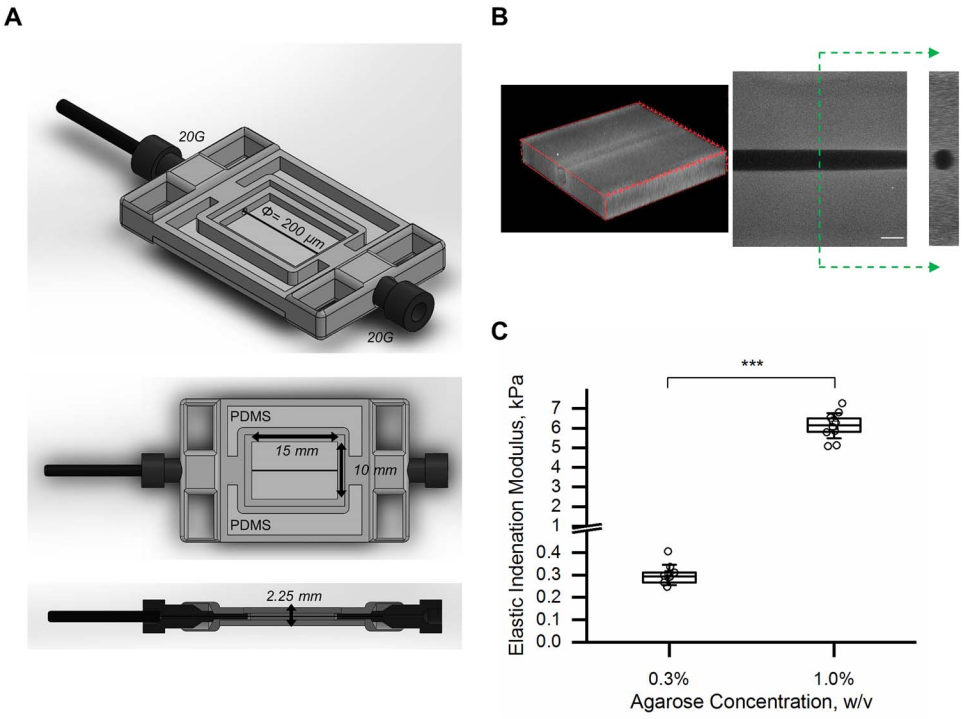

Figure 2. Fabrication of the VLCM. (A) The shorter 3D printed template used to aid in the fabrication of cylindrical microchannels in agarose hydrogels. A 200 μm-diameter rod was suspended across the rectangular opening into which agarose was dispensed and gelled. Removal of the rod formed the VLCM. (B) A 3D reconstruction and orthographic projections (top and side) of the VLCM. Fluorescent microbeads were mixed into the agarose prior to gelation to confirm the integrity of the microchannel. Scale bar is 200 μm. (C) Elastic indentation moduli of agarose hydrogels at different concentrations. Data are representative of $n \geq 3$ from three independent experiments. *** denotes $P < 0.001$.

not subsequently replaced during the growth period. Brightfield images of the tumor emboli were taken daily using an Axio Vert.A1 (Zeiss).

Micro-computed tomography (microCT)

To examine the three-dimensional morphology of tumor emboli grown in both stiff and soft matrix VLCMs, we imaged samples using microcomputed tomography (microCT). Samples were incubated in an iodine solution overnight (Acros). A microCT scan was acquired using a vivaCT 40 (Scanco Medical) at 45 kVp and 177 μA with a pixel size of 10.5 μm × 10.5 μm × 10.5 μm. IMARIS software (Oxford Instruments) was used to reconstruct the scan.

Inhibition of force generation via drugs

To examine the effects of inhibiting force generation, we used the Rho-associated protein kinase (ROCK) inhibitor Y-27632 (Enzo Life Sciences) at 100 μM and the myosin II inhibitor blebbistatin (Enzo Life Sciences) at 10 μM. For unconstrained samples, spheroids were grown for 3 days to allow compaction, and then the media was replaced with media containing a drug, the solvent of a drug (water (H_2O) for Y-27632 or dimethyl sulfoxide (DMSO) for blebbistatin), or no drug (normal). Samples were then cultured for seven more days before being mechanically tested. Similarly, for microchannel-constrained samples, cells were grown in the channels until they reached the diameter of the microchannel, and then the emboli-containing samples were transferred into 6-well plates with media containing a drug, the solvent of a drug, or no drug. Samples were then cultured for 10 more days for analysis.

Mechanical characterization of agarose and tumor spheroids

To characterize the stiffness and stress relaxation properties of hydrogels and tumor spheroids, milli-scale indentation and compression were performed, respectively, using a high-precision piezo-electric actuator-controlled system (CellScale, Canada). For indentation of hydrogel samples, indenters were constructed by gluing borosilicate glass spheres (radius R = 1.5 mm) to the ends of tungsten beams (Young's modulus E_b = 411 GPa) with circular cross-sections. For parallel-plate compression of spheroid samples, stainless-steel plates were fixed to the ends of the tungsten beams. The opposite end of the respective beam was then fixed onto a piezo-controlled positioning system.

A camera is positioned such that the displacement of the free end of the cantilevered beam, and hence displacement of the sample (indentation depth, d), was measured optically. Knowing the displacement of the piezo base (z) allowed the cantilevered beam deflection (δ) to be calculated as $\delta = z - d$. Force (F) was determined from the deflection of the beam using the Euler-Bernoulli beam bending theory for a cantilevered beam loaded at the free end, which is dependent on other parameters of the beam including length (L), Young's modulus (E_b), and cross-sectional area moment of inertia (I), $F = 3\delta E_b I/L^3$. The force measurements were plotted against indentation depth. To estimate sample elastic indentation modulus (E_i), the experimental

force-indentation depth curves were fit to the Hertz contact equation, which estimates the force resulting from contact between a spherical body and a flat surface:

$$F = \frac{4}{3}\frac{E_i R^{1/2}}{(1-\nu^2)}d^{3/2}$$

Here, R is the radius of the spherical indenter and ν is the sample's Poisson's ratio (approximated here to be 0.49, consistent with typical reported values for incompressible soft tissues [34–36]). The elastic indentation modulus of each sample was determined using a linear least-squares method applied by a customized MATLAB code, which identified the value for modulus that minimized the error between the raw data and model Hertz curve.

For milli-indentation of agarose gels, indentation and retraction rates were kept constant at 4 μm/s. To maintain elastic half-space assumptions, samples were indented to 10% of their measured height. All samples were glued to the stage to prevent floating and were tested in a PBS fluid bath at room temperature (~23°C). At least three different locations were tested per sample.

For milli-compression of spheroids, samples were gently pipetted into the PBS fluid bath and tested at room temperature. A minimum of five spheroids was tested within each treatment group for each independent experiment. All spheroids were compressed to 20% deformation of their initial height, which induced a magnitude of force great enough to be captured by the cantilever beams according to their respective force resolutions while still maintaining elastic half-space assumptions [37]. A full test consisted of a compression phase, during which the deformation rate at the sample was 5 μm/s, followed by a 10-s hold phase in which the beam was held to a fixed sample deformation to assess the stress relaxation response.

Soft tissues and their hydrogel simulants often exhibit viscoelastic responses to loads [34, 38–40]. In different studies, MCTSs, in particular, have been shown to exhibit combinations of elastic, viscous or plastic material behavior owing to the time scale of testing or analysis and the diverse properties of their constituents. A response similar to an elastic solid is expected at short times, with viscous and plastic flow responses occurring at long times, the latter due to cell rearrangements [41, 42]. Some studies have modeled MCTSs as viscous liquids [43] noting the independence of compression magnitude and surface tension, but have found that exceptions exist within an experimental population. Taking into account initial elastic responses coupled with liquid-like behaviors such as rounding up and spreading, other studies have modeled cell spheroids as viscoelastic liquids [44]. Finally, others have determined that cellular aggregates are best modeled as elasto-visco-plastic solids, due to a more pronounced solid-like behavior followed by plastic rearrangements [42, 45]. Here, we characterized our cellular spheroids as viscoelastic solids, focusing on shorter times of testing, as we aimed to capture the contribution of the active process of actomyosin contractility on the intrinsic tumor cell aggregate mechanical properties. This furthermore allowed a direct comparison to the agarose hydrogels.

To assess the stress relaxation response (Supplementary Figure S2), we held a constant deformation during mechanical testing and subsequently chose a set of parameters that described this viscoelastic behavior. The first of these properties, half-time relaxation ($t_{1/2}$), defines the amount of time required to reach half of the total force that is relaxed within the sample, providing a measure of how quickly the sample relaxes. A second viscoelastic property we used was the ratio of steady-state, relaxed modulus (E_{ss}) to indentation modulus (E_i). This property provided a measure for how much the sample relaxed, with lower ratios indicating a greater degree of relaxation. Steady-state modulus (E_{ss}) was found by substituting the steady-state, relaxed value of force obtained during the hold phase—at which point the sample had reached a new equilibrium—into the Hertz contact equation [34, 35].

Western blot

To assess the expression of the force-generating protein myosin IIa, western blotting was performed. HCT116 and SUM149PT whole cell lysates were isolated from spheroids grown for 7 days using mammalian protein extraction reagent (M-PER; ThermoFisher) following manufacturer protocols. Samples were treated with Bolt LDS Buffer (ThermoFisher) and Bolt reducing agent (ThermoFisher) and were heated to 70°C for 10 min. Protein separation was done through electrophoresis using a Bolt 8% bis-tris gel (ThermoFisher) with wells loaded with 10 μg of protein. Subsequently, proteins were transferred onto a nitrocellulose membrane and then blocked overnight while shaken at 4°C in TBST-5% BSA—a TBS Tween-20 (TBST; ThermoFisher) solution containing 5% bovine serum albumin (BSA; Sigma).

Primary antibodies for myosin IIa (1:5000; Cell Signaling Technology) and GAPDH (1:15000; Cell Signaling Technology) were diluted in TBST-5% BSA. The diluted primary antibodies were applied to appropriate sections of the membrane overnight while on a shaker at 4°C. Membrane sections were washed overnight while shaken at 4°C in TBST. Horseradish peroxidase-conjugated secondary antibodies (Cell Signaling Technology) diluted in TBST-5% BSA were then applied for 1 h. Secondary antibody dilutions were as follows: myosin IIa at 1:10000 and GAPDH at 1:15000. Bound antibodies were detected using SuperSignal West Pico PLUS Chemiluminescent Substrate (ThermoFisher). Imaging was performed using a Chemidoc XRS+ system (BioRad). Quantification of band parameters was performed using the associated Image Lab software (BioRad).

Contractility assay

To assess the contractile ability of the two cell lines, they were separately encapsulated in collagen gels and allowed to contract the gels over 24 h. A collagen precursor solution was prepared from a monomeric collagen solution extracted from rat tails as described in Gong *et al.* [46]. The collagen precursor was neutralized following common protocols available for commercially available products with ×10 PBS, 2 mM NaOH and H_2O while on ice. The neutralized collagen precursor was diluted with the appropriate media to a final concentration of 1.5 mg/ml. This solution was then used to resuspend a cell pellet of the respective cell line to achieve a cell density of 250 000 cells/ml. The cell suspension was deposited in a 24-well plate with 500 μl per well and allowed to gel for 1 h in an incubator at 37°C and 5% CO_2. After gelation, 500 μl of media (with and without drugs or their solvents) was added to each well. Each gel was carefully detached from the walls of the well plate using a pipette tip and gentle shaking. The plate was cultured in the incubator for 24 h, after which the cell-containing

collagen gels were imaged. The areas of the gels were measured using ImageJ.

Image analysis

CellProfiler was used to acquire the mean radius of samples grown without a vessel-like constraint [47]. A spherical shape was assumed, and the volume of the spheroids was calculated as $V = \frac{4}{3}\pi r^3$.

ImageJ was used to acquire the major and minor axes of samples grown under a vessel-like constraint. For emboli constrained by the soft or stiff matrix channels (with and without drugs), a cylindrical shape was assumed, and the volume of these emboli was calculated as $V = \pi r^2 l$, where r is the radius of the circular cross-section (minor axis) and l is the length of the major axis. For emboli that were not constrained by the soft or stiff matrix channels, an oblate ellipsoidal shape was assumed, and the volume of the emboli was calculated as $V = \frac{4}{3}\pi a^2 b$, where a is the radius of the major axis and b is the radius of the minor axis.

Statistics

All scatter plots and bar graphs are reported as mean ± standard error of the mean and were plotted using OriginPro (OriginLab). Statistical differences between the growth conditions via constraint or drug inhibition were determined by one-way ANOVA tests with Tukey post hoc using OriginPro (OriginLab). Differences were considered significant at $P < 0.05$.

RESULTS

Fabrication of the VLCM: molding microchannels in stiff or soft hydrogels

Lymphatic vasculature can be generalized as tubular organs within the connective tissue of the body; thereby, our VLCM consisted of a cylindrical channel within a hydrogel matrix. To construct the VLCM, a microchannel was formed by templating a stainless-steel rod within an agarose matrix. The rod had a diameter of 200 μm, which is approximately the diffusion limit of oxygen in tissue [48, 49] and is similar in diameter to that of collecting lymphatic vessels [50, 51]. Two variants of a 3D-printed frame were used to suspend the rod: a short template for the soft matrix and a long template for the stiff matrix (Fig. 2A and Supplementary Figure S1, respectively). The integrity of the microchannel was confirmed by imaging of a test sample embedded with fluorescent nanoparticles (Fig. 2B). The hydrogel matrix used was agarose, which was chosen for its bioinert properties that prevent cell adhesion and degradation, its nanoporosity that prevents cell migration and invasion, and its wide range of stiffness that may be tuned by changing the agarose concentration [23, 24, 52]. Agarose concentrations of 1.0% (w/v) and 0.3% (w/v) were used to mimic excessive (stiff) and normal (soft) tissue stiffness, respectively (Fig. 2C). The elastic modulus of agarose at 1.0% was measured to be 6130 ± 213 Pa, while 0.3% agarose had an elastic modulus of 302 ± 11 Pa. These stiffness values represent the range of measurements that have been made on cancerous and healthy human colon and breast tissues, corresponding to the tissue origins of the cell lines that we used in this study. Measurements on cancerous colon tissues have indicated a range in modulus between 1 and 4.4 kPa, while normal colon tissues typically have moduli in the range of 0.5–1 kPa [53, 54]. Cancerous and healthy breast tissues are reported to possess moduli in the ranges of 1.6–12 kPa and 1.1–1.8 kPa, respectively [55–57]. We used the VLCM developed here to isolate the effects of the geometric constraint and mechanical stiffness on the growth of tumor emboli without having to account for matrix modifications beyond those due to tumor volumetric growth.

Stiffness of the VLCM matrix influences tumor emboli morphology

Using both human colon cancer cells (HCT116) and human breast cancer cells (SUM149PT), we first compared the growth of tumor spheroids (no mechanical constraint) to the growth of tumor emboli in our VLCM with either a stiff or soft agarose matrix. We first noted that both cell lines had similar doubling times when cultured as monolayers in flasks (Supplementary Figure S3). Growing as spheroids, both cell lines maintained a projected circular shape, commonly seen in other studies (Fig. 3A and B) [22, 58–60]. Both cell lines also produced spheroids that exhibited similar growth dynamics, increasing in volume first exponentially followed by a reduction in growth rate. We observed this reduction in growth rate after ~2 weeks by both cell lines at tumor spheroid diameters of about 720 ± 50 μm and 560 ± 30 μm, for the HCT116 and SUM149PT cell lines, respectively. The reduced growth rate has been attributed to cell death and senescence within the spheroids due to the inability of nutrients to diffuse into, and waste to diffuse out of, inner regions, leaving proliferation to a thin peripheral region. This thin peripheral region of proliferating cells in unconstrained tumor spheroids results in diametral growth rates tending toward linear with time and, therefore, volume increases as the cube of time. Such growth dynamics of tumor spheroids have been extensively studied over many years [61–63] as spheroids have been a valuable preclinical model of early, prevascular tumor growth [61].

When grown as emboli within the stiff matrix VLCM, the emboli were confined to and elongated within the tubular geometry of the microchannel (Fig. 3A and B, Supplementary Figure S4B). The stiff matrix restricted the expansion of the HCT116 tumor emboli circumferentially, forcing the cells to grow along the channel length. The SUM149PT tumor emboli were also constrained circumferentially, although they bulged slightly against the stiff matrix. The elongated tumor emboli in the stiff matrix VLCM often exceeded the length of the short template, necessitating the longer template to be able to measure growth over the entire culture period. The volumetric growth curves for either cell line in the stiff matrix VLCM do not reach an obvious reduced growth rate after 20 days of growth, and the emboli volumes significantly exceeded those of the spheroids grown without constraint (Fig. 3C and D). Furthermore, the HCT116 emboli volumes significantly exceeded those of the SUM149PT emboli. Integrating the volumetric growth—assuming a surface proliferation rate determined by a fit of the unconstrained spheroid experimental growth curve—predicts slower volumetric growth of an unconstrained cylinder than what is observed when it is constrained in the VLCM geometry (black dotted lines; Figs 3C and D, Supplementary Figure S5). The constraint of the VLCM geometry seems to have conferred a growth advantage to the cells, likely because the stiff matrix surrounding the 200 μm-diameter channel physically restricted the tumor emboli from growing larger (in the cross-section of the channel) than the diffusion limit distance.

As the elastic modulus of the stiff agarose exceeds that of most healthy soft tissues, we repeated the experiment but with cylindrical channels molded into soft agarose that are

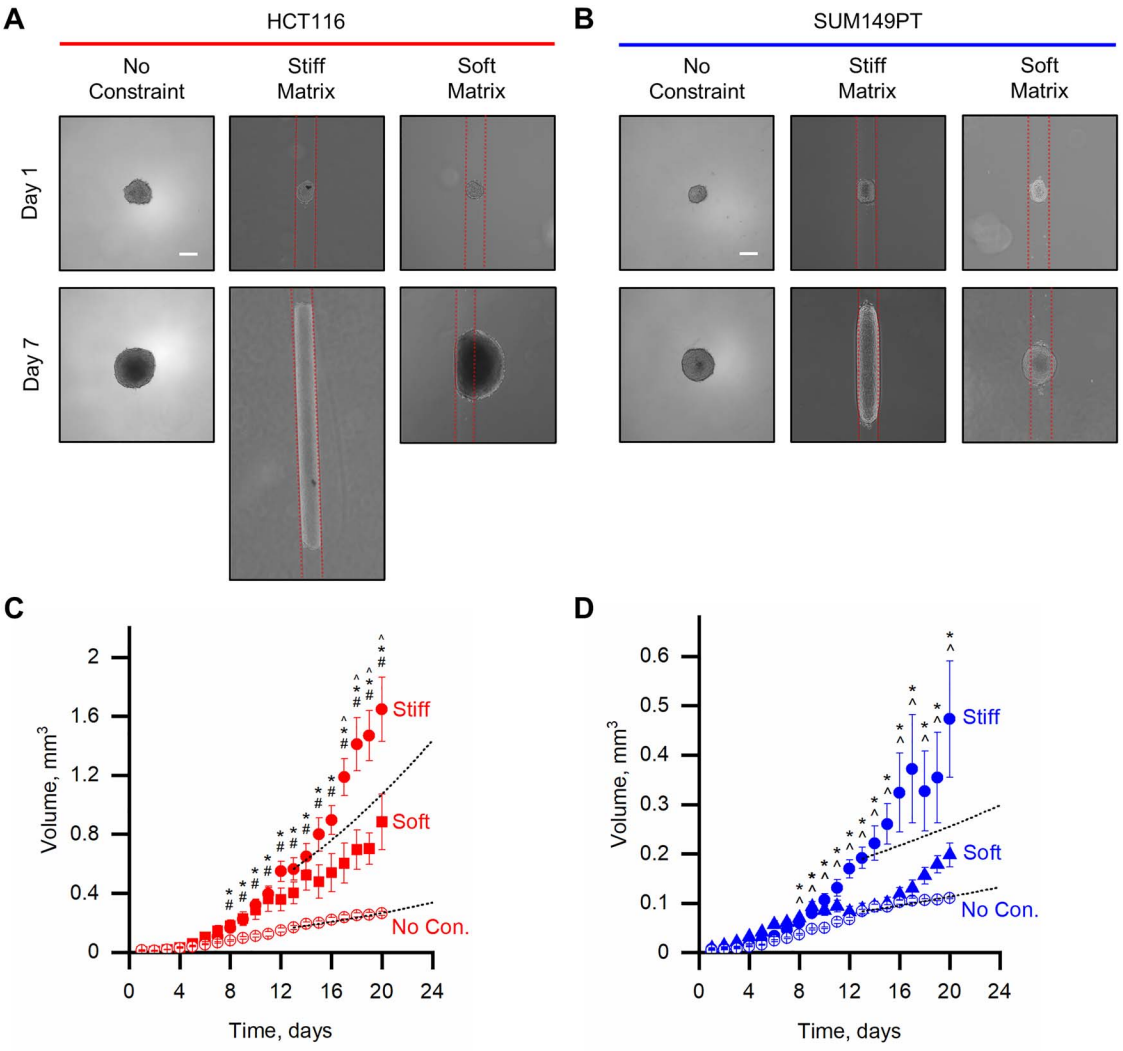

Figure 3. Stiffness of the VLCM matrix influences tumor emboli growth and morphology. (A) Phase-contrast images of HCT116 cells grown without constraint as spheroids (left), within the stiff matrix VLCM (middle), and within the soft matrix VLCM (right). (B) The same as (A) except for SUM149PT cells. (C) Tumor cell aggregate volumes over a growth period of 20 days of HCT116 spheroids (No Con.) and emboli in both the soft matrix VLCM (Soft) and stiff matrix VLCM (Stiff). Dotted lines are calculated fits (No Con.) and corresponding calculated predictions (Stiff) of unconstrained tumor cell aggregate growth assuming a proliferative surface layer of cells (Supplementary Figure S5). (D) The same as (C) but for SUM149PT cells. Scale bars in (A) and (B) are 200 μm. All data points are presented as mean ± SEM. $*P < 0.05$ for Stiff compared to No Con. $^{\#}P < 0.05$ for Soft compared to No Con. $^{\wedge}P < 0.05$ for Stiff compared to Soft.

closer to normal tissue stiffness [64]. Interestingly, in this soft matrix VLCM, emboli growth was not confined to the cylindrical channel as in the stiff matrix VLCM. Rather, after forming a spheroid that filled the diameter of the channel, the tumor emboli grown from both cell lines eventually bulged into the matrix (Fig. 3A and B). Although they were growing against the soft matrix and did not significantly elongate along the channel, the emboli in the soft matrix VLCM from both cell lines had intermediate growth rates between the unconstrained spheroids and emboli in the stiff matrix VLCM (Fig. 3C and D). They also did not reach an obvious reduced growth rate after 20 days.

The growth dynamics and tumor emboli shapes in the soft matrix VLCM, similar to the stiff matrix VLCM, were cell-line dependent. HCT116 emboli grown in the soft matrix VLCM increased in volume faster than when grown as spheroids, but slower than when grown as emboli in the stiff matrix VLCM (Fig. 3C). In contrast, SUM149PT emboli grown in the soft matrix VLCM did not increase in volume significantly faster than when grown as spheroids until the time that the spheroids reached the reduction in their growth rate (Fig. 3D). The SUM149PT emboli grown in the stiff matrix VLCM, however, still increased in volume fastest as compared to the emboli in the soft matrix VLCM and spheroids. The shape to which the emboli grew were also different for the two cell lines. The HCT116 emboli expanded from the channel into a roughly oblate ellipsoidal shape (Fig. 3A, projection, and Supplementary Figure S4A), whereas the SUM149PT emboli maintained a more circular projection throughout the growth period (Fig. 3B). Together, we demonstrated that imposing a vessel-like geometrical constraint on the growth of tumor cell aggregates significantly impacted the rates and shapes of their growth. In addition to the cylindrical channel geometry, the stiffness of the matrix was a determinant of the rate and shape of tumor cell aggregate growth, demonstrating an apparent mechanosensitivity of the tumor cells.

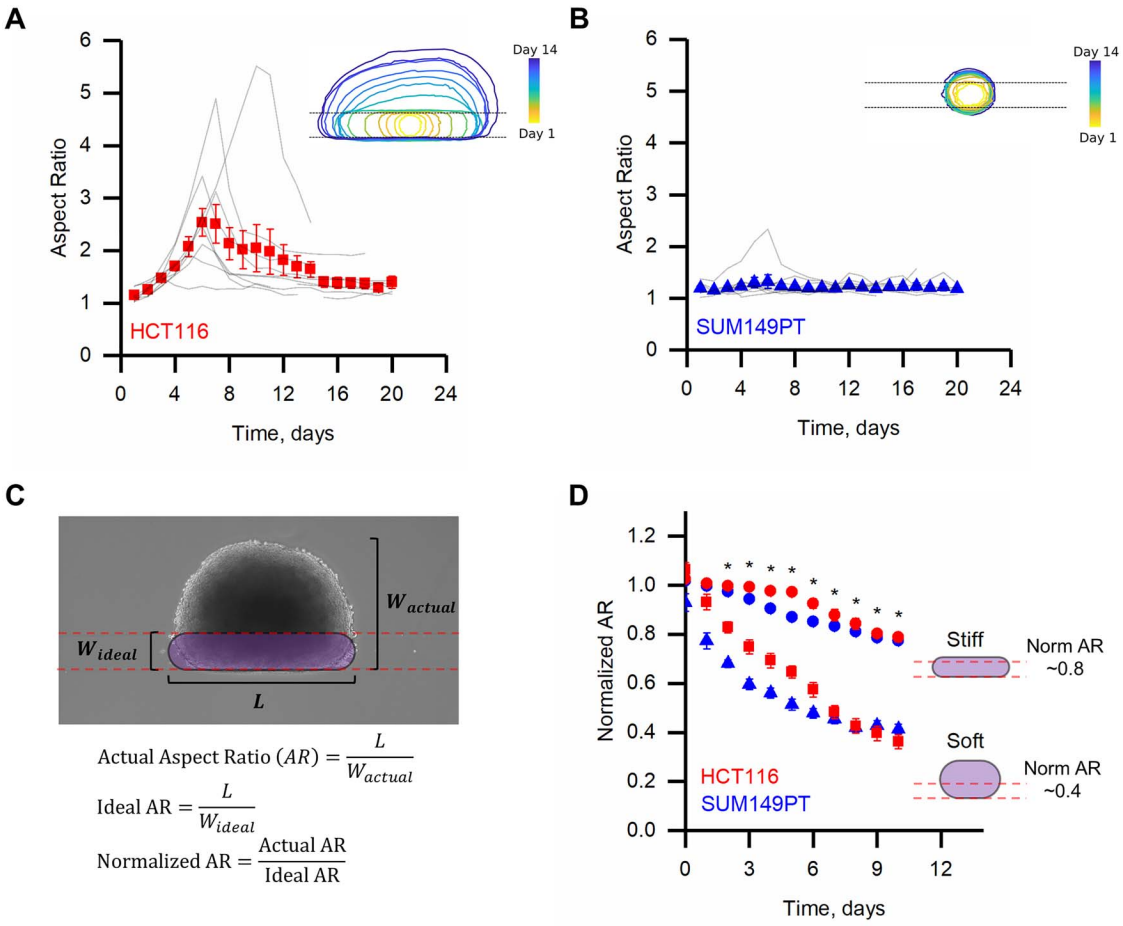

Figure 4. Mechanosensitivity to a soft matrix VLCM constraint leads to differences in tumor emboli morphology. Average aspect ratio of (A) HCT116 tumor emboli (red, squares) and (B) SUM149PT tumor emboli (blue, triangles) grown in the soft matrix VLCM overlaid onto aspect ratios of individual tumor emboli (grey) over 20 days. Inset diagrams depict the morphology of average tumor emboli, of the respective cell type, over a 14 days period. (C) Schematic illustrating the 'normalized' aspect ratio. The ideal width (w_{ideal}) is set to be the diameter of the VLCM (200 μm) and the length (L) is the major axis. (D) Normalized aspect ratios of both HCT116 and SUM149PT emboli grown in soft and stiff matrix VLCMs (HCT116, red: Stiff = circles, Soft = squares; SUM149PT, blue: Stiff = circles, Soft = triangles). At least five samples ($n \geq 5$) are depicted for all time points in each graph. All data points are presented as mean ± SEM. ∗ denotes $P < 0.05$ for Stiff compared to Soft.

As the overall shapes of the tumor emboli grown within the soft matrix VLCM were drastically different, we characterized their morphologies as a function of time. Examples of projected tumor outlines are plotted as heat maps as a function of time in the insets of Fig. 4A and B for HCT116 and SUM149PT cells, respectively. After filling the microchannel, the HCT116 emboli elongated to a relatively high aspect ratio, most between 2 and 5 (Fig. 4A), along the length of the channel of the soft matrix VLCM. The elongation continued until around day 7, when they bulged out of the channel and into the agarose matrix, reducing their aspect ratio (Fig. 4A). In contrast, the SUM149PT cells maintained a uniform, round projection seemingly without being influenced by the channel geometry as their aspect ratio was almost 1 throughout the culture period (Fig. 4B). These observations suggest that the HCT116 emboli were more sensitive to the geometry of the soft matrix VLCM—initially growing along the open channel—as compared to the SUM149PT emboli that appeared unaffected by the presence of the soft matrix.

To quantify the amount of bulging into the matrix, we defined a normalized aspect ratio to compare the actual bulged shape to an ideal, channel-confined tumor (Fig. 4C). The ideal aspect ratio is the length that the tumor grew along the channel divided by the channel width. The actual aspect ratio is the length that the tumor grew along the channel divided by its actual width. The normalized aspect ratio (actual/ideal) decreases with increased bulging against the microchannel. Plotting the average normalized aspect ratio for emboli from each cell line in soft and stiff matrix VLCM (Fig. 4D) highlights our observation that in no case was bulging fully restricted. The stiffer matrix, however, provided significantly more constraint. Also clearly illustrated is the immediate bulging of the SUM149PT emboli grown in the soft matrix VLCM (Fig. 4D). This analysis of the time-course of the shape development of the tumor emboli in the soft matrix VLCM reveals that HCT116 emboli were initially sensitive to the mechanical constraint, while the SUM149PT emboli were not.

Tumor spheroid biomechanical properties are products of force-generating mechanisms

To account for the dissimilarity in the evolution of tumor emboli shapes between cell lines, we hypothesized that their elastic moduli (E_{emb}) were significantly different and, therefore, they possessed different magnitudes of mechanical mismatch

with the matrix (E_{VLCM}) of the VLCM ($E_{VLCM}/E_{emb} \neq 1$). In fully embedded tumor models, this mechanical mismatch has been shown to determine the magnitude of elastic strain energy in the growing tumor-gel system, which in turn drives the shape of tumor cell aggregate growth [23]. Specifically, when the embedded tumor is softer than the agarose matrix, it will grow into an ellipsoid whereas when the embedded tumor is stiffer than the matrix, it will grow into a sphere. Therefore, we hypothesized that the SUM149PT spheroids were stiffer ($0 < E_{VLCM}/E_{emb} < 1$), whereas the HCT116 spheroids were softer ($E_{VLCM}/E_{emb} > 1$), than the soft matrix.

We measured the mechanical properties of HCT116 and SUM149PT tumor spheroids after 10 days of growth using parallel-plate compression. Indeed, the measured elastic modulus of the HCT116 ($E_{emb,\,HCT} = 117 \pm 31$ Pa) and SUM149PT ($E_{emb,\,SUM} = 1195 \pm 332$ Pa) spheroids (Fig. 5A) seemingly supported our hypothesis. In the stiff matrix VLCM, the mechanical mismatch between the matrix surrounding the channel and the emboli would be $E_{VLCM}/E_{emb} = 52$ for the HCT116 and 5.1 for the SUM149PT emboli. In the soft matrix VLCM, the HCT116 emboli were initially confined to the channel, $E_{VLCM}/E_{emb} = 2.6$, while the SUM149PT were not, $E_{VLCM}/E_{emb} = 0.25$. After an average of about 7 days of growth in the soft matrix VLCM, when they start to bulge into the matrix, it is likely that the HCT116 tumor emboli stiffened in response to the constraint. We and others have observed the formation of a thick actin shell surrounding tumor cell aggregates when they are embedded and allowed to grow in hydrogels with elastic moduli similar to or stiffer than the aggregates, but not when the hydrogels are softer (Supplementary Figure S6, [65]). The development of such a thick actin shell has been shown to lead to an increase in aggregate stiffness [65, 66].

Cell aggregate stiffness has been linked to (i) actomyosin-generated tension in embryonic tissues and in epithelial sheets as well as to (ii) excessive extracellular matrix deposition and crosslinking in disease processes such as cancer [67–71]. Cells in spheroid culture produce ECM proteins [62, 72, 73]; however, it is believed that they are not rigid and load-bearing [73]. Therefore, we concluded that tension generation via actomyosin contractility was likely the major determinant of the stiffness of the tumor spheroids. Seeming to corroborate this conclusion, western blot analysis showed that the myosin IIa expression of SUM149PT cells was 10 times higher than that of HCT116 cells (Fig. 5B) and SUM149PT cells exhibited significantly higher force generation in a collagen-gel contraction experiment (Supplementary Figure S7A).

To explore whether actomyosin contractility significantly contributes to the stiffness of the tumor spheroids, we tested whether their stiffness could be modulated via perturbations of myosin-related force generation through two commonly targeted routes: the ROCK pathway and myosin II. The ROCK pathway is associated with the regulation of cell shape, movement and contractility by phosphorylation of myosin light chains, which increases myosin II ATP activity [74–76]. Myosins are motor proteins primarily associated with contraction and motility when they work in concert with actin filaments. Myosin II is specifically responsible for cellular contraction [77–79]. Spheroids that had stably aggregated after 3 days were treated with drugs targeting either ROCK—using Y-27632 (100 μM)—or myosin II directly—using blebbistatin (10 μM). The growth of the tumor spheroids was monitored over 7 days after treatment and then their stiffness was measured. The growth of the HCT116 spheroids was not affected by either inhibitor as all spheroids reached diameters in the same order as the normal, untreated spheroids (Supplementary Figure S8A). In terms of their stiffness, however, both the ROCK inhibitor (Y-27632) and blebbistatin significantly reduced their average stiffness by 60% and 43%, respectively (Fig. 5C). In contrast, both inhibitors hindered the growth of the SUM149PT spheroids, as these samples reached diameters about 100-μm smaller than untreated and control samples (Supplementary Figure S8B). The introduction of Y-27632 reduced the average stiffness of the SUM149PT spheroids by 57%, similar to the effects on HCT116 spheroids. However, blebbistatin interestingly had no effect on the average stiffness of the SUM149PT spheroids (Fig. 5D). A similar observation of the effects of blebbistatin on SUM149PT cells was made in a collagen-gel contraction experiment: it did not inhibit contractility of SUM149PT cells whereas the ROCK inhibitor did (Supplementary Figure S7B). Together, these results indicate that inhibition of myosin-related force generation through either the ROCK pathway or myosin II also decreases the elastic moduli of tumor spheroids, with the exception of blebbistatin-treated SUM149PT spheroids, which were not significantly affected.

Myosin inhibition increases stress relaxation in tumor spheroids

In addition to effects on the elastic moduli of the spheroids, treatment of the spheroids with the ROCK inhibitor and blebbistatin also altered their viscoelastic properties. We used the stress relaxation behavior of the agarose and MCTSs to quantify their steady-state, relaxed modulus and half-time of relaxation. The steady-state elastic modulus of both the agarose hydrogels and the untreated MCTSs was between 22% and 27% of the indentation modulus (E_{ss}/E_i, Fig. 5E). For HCT116 spheroids treated with either inhibitor, the steady-state modulus was slightly, although significantly, decreased with respect to the indentation modulus. In contrast, the SUM149PT spheroids treated with either inhibitor displayed a large drop in steady-state modulus compared to the untreated spheroids. The ratio E_{ss}/E_i for the SUM149PT spheroids was decreased to 0.12 ± 0.04 and 0.12 ± 0.02 for the blebbistatin and ROCK inhibitor, respectively, from 0.24 ± 0.01 for the untreated SUM149PT spheroids. Taking into account, the relaxation in the mechanical mismatch for one of these cases, SUM149PT spheroids treated with the ROCK inhibitor, we observed that this increased relaxation switched E_{VLCM}/E_{emb} for the soft matrix VLCM from less than one, $(E_{VLCM}/E_{emb})_i = 0.59$, to greater than one, $(E_{VLCM}/E_{emb})_{ss} = 1.2$. The relaxation rates of all MCTSs were also increased with either drug treatment, but the relaxation half-times remained within the range of 1.7 to 2.0 s for all MCTSs (both untreated and drug-treated) whereas, for agarose relaxation, half-times were between 30 and 50 s (Supplementary Figure S9). Thus, in addition to decreasing the elastic moduli of most tumor spheroids, the ROCK and myosin II inhibitors increased the magnitude and rate of stress relaxation of all tumor spheroids. The one case where no effect was made on elastic modulus was SUM149PT spheroids treated with blebbistatin.

Inhibition of force generation leads to the constraint of emboli growth in the soft matrix VLCM

Since the ROCK and myosin II inhibitors increased the compliance and/or the degree of relaxation of the HCT116 and SUM149PT spheroids, they effectively increased the magnitude of mechanical mismatch between the spheroids and the VLCM

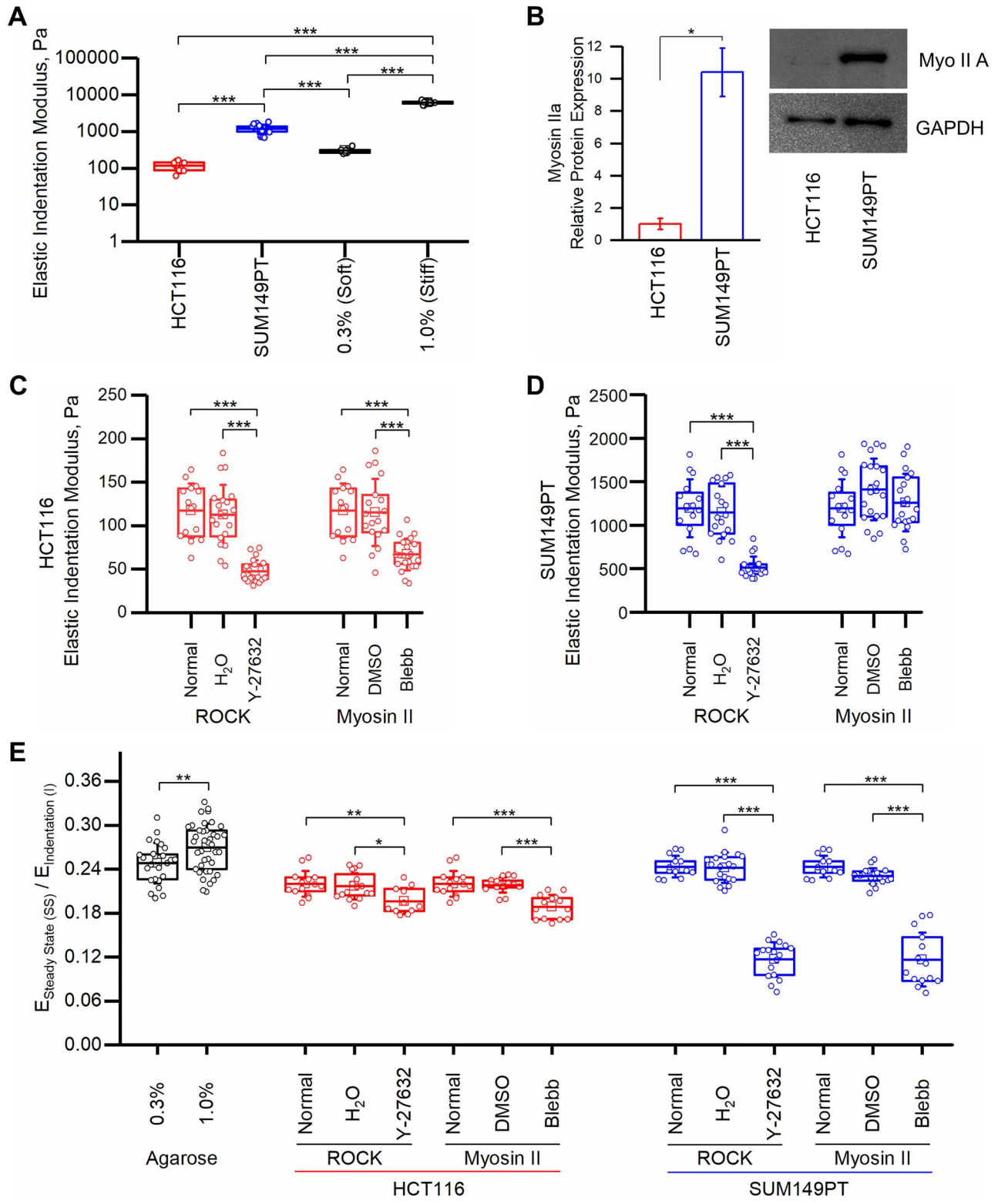

Figure 5. Inhibition of force generation leads to shifts in tumor spheroid biomechanics. (A) Elastic moduli of HCT116 and SUM149PT spheroids grown for 7 days compared to the stiffness of the soft and stiff agarose matrices. (B) Relative expression and representative images of western blots of myosin IIa and GAPDH from HCT116 and SUM149PT spheroids over three independent experiments. (C) Elastic indentation moduli of HCT116 spheroids grown with and without drugs after 7 days of treatment. (D) Same as (C), but for SUM149PT. (E) Ratio of steady-state moduli over elastic indentation moduli of agarose as compared to HCT116 and SUM149PT spheroids with and without drug treatments. Box plots are representative of three independent experiments with $n \geq 5$ samples each. *, **, and *** denote $P < 0.05$, $P < 0.01$, and $P < 0.001$, respectively.

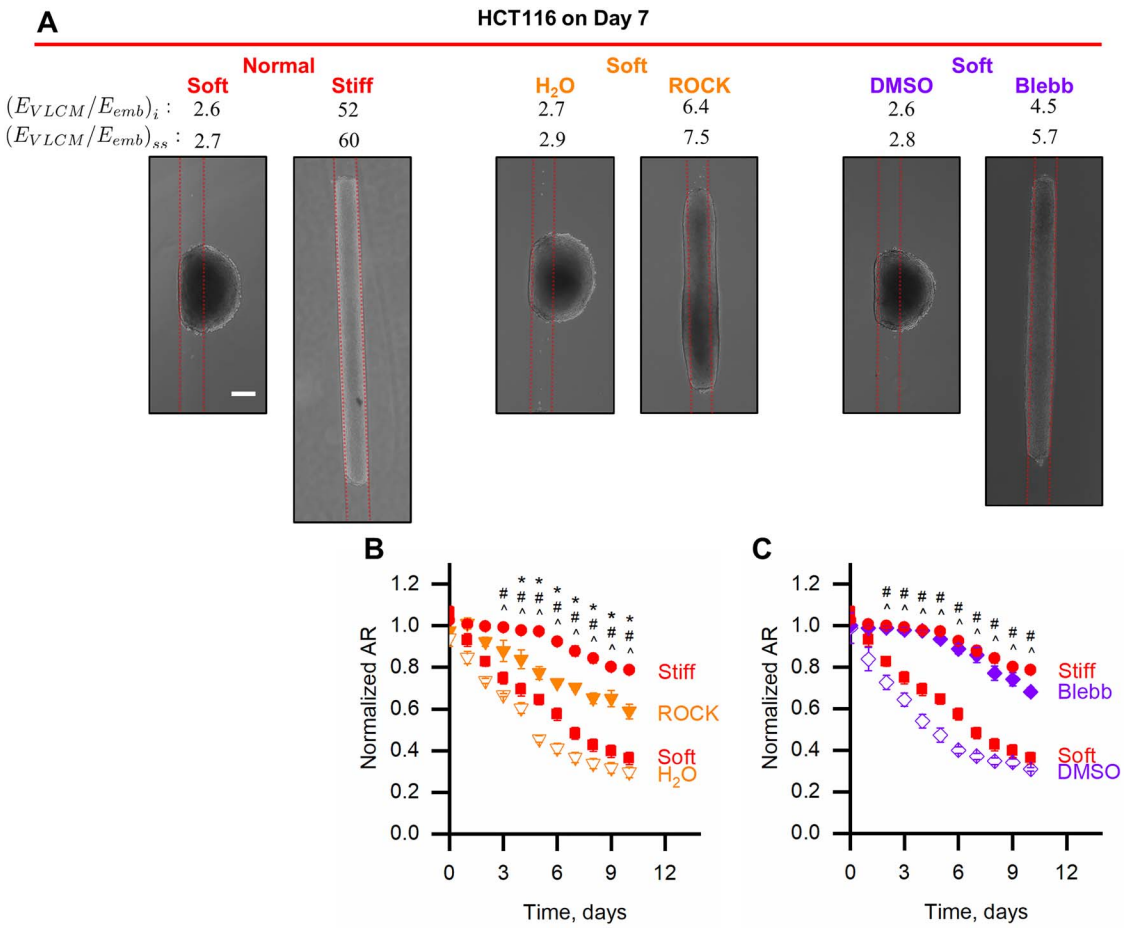

Figure 6. ROCK and myosin II inhibition lead to increased confinement of HCT116 emboli in the soft matrix VLCM. (A) Representative phase-contrast images of HCT116 emboli grown without drug treatment (normal) or with a drug (and compared with its control) in the soft matrix VLCM. All images are taken on Day 7. Red dotted lines denote the boundaries of the vessel-like constraint. Scale bar is 200 μm. (B) Normalized aspect ratio of HCT116 emboli treated with the ROCK inhibitor (orange triangles) compared to those grown under soft and stiff matrix VLCMs (red squares and circles, respectively). (C) Same as (B), but with blebbistatin (purple diamonds). Data are representative of $n \geq 3$. $*P < 0.05$ for drug treatment compared to Stiff. $^{\wedge}P < 0.05$ for drug treatment compared to Soft. $^{\#}P < 0.05$ for drug treatment compared to control.

matrix. We, therefore, hypothesized that treatment of the emboli with these inhibitors would lead to increased confinement of growth in the soft matrix VLCM. To test this hypothesis, the inhibitors were introduced to tumor emboli within the soft matrix VLCM once they grew to the diameter of the channel. Emboli growth and morphologies were measured and monitored over a period of 10 days.

The drug treatment did not appear to affect the growth of the tumor emboli as their volumes were not significantly different from the untreated emboli (Supplementary Figures S8C and S8E). However, when treated with either inhibitor, tumor emboli from both cell lines displayed increased confinement, to different degrees, of growth along the channel in the soft matrix VLCM (Fig. 6A). Treatment of HCT116 emboli with the ROCK inhibitor lessened emboli bulging into the soft matrix as compared to untreated (normal) emboli, with normalized aspect ratios of 0.70 ± 0.02 and 0.48 ± 0.08 on Day 7, respectively (Fig. 6B). In contrast, blebbistatin treatment recovered the level of HCT116 emboli confinement to that of the untreated emboli in stiff matrix VLCM (Fig. 6C).

Growth of the SUM149PT emboli in the soft matrix VLCM was more sensitive to the ROCK inhibitor than blebbistatin (Fig. 7A). ROCK inhibitor-treated SUM149PT emboli grew along the channel similarly to untreated emboli in the stiff matrix VLCM (Fig. 7B). On the other hand, the SUM149PT emboli treated with blebbistatin appeared to be significantly less affected by the drug, forming emboli with normalized aspect ratios similar to those of the untreated and control samples in the soft matrix VLCM (Fig. 7C). However, a slight elongation along the microchannel was observed under the treatment with blebbistatin (Fig. 7A). As with the HCT116, the volumes of the SUM149PT emboli were not significantly affected (Supplementary Figures S8D and S8F). Together, we demonstrated that the increase in the mechanical mismatch between the VLCM matrix and the tumor emboli—due to decreased stiffness *or* increased relaxation of the tumor cell aggregates after treatment with a ROCK or myosin II inhibitor—correlated with increased confinement of emboli growth in the soft matrix VLCM. In two cases (ROCK-treated SUM149PT and blebbistatin-treated HCT116), the level of confinement was nearly as high as that provided by the stiff matrix VLCM.

DISCUSSION

In this study, we examined the morphological response of a tumor cell aggregate growing within a vessel-like constraint as it would in the context of a tumor embolus. We

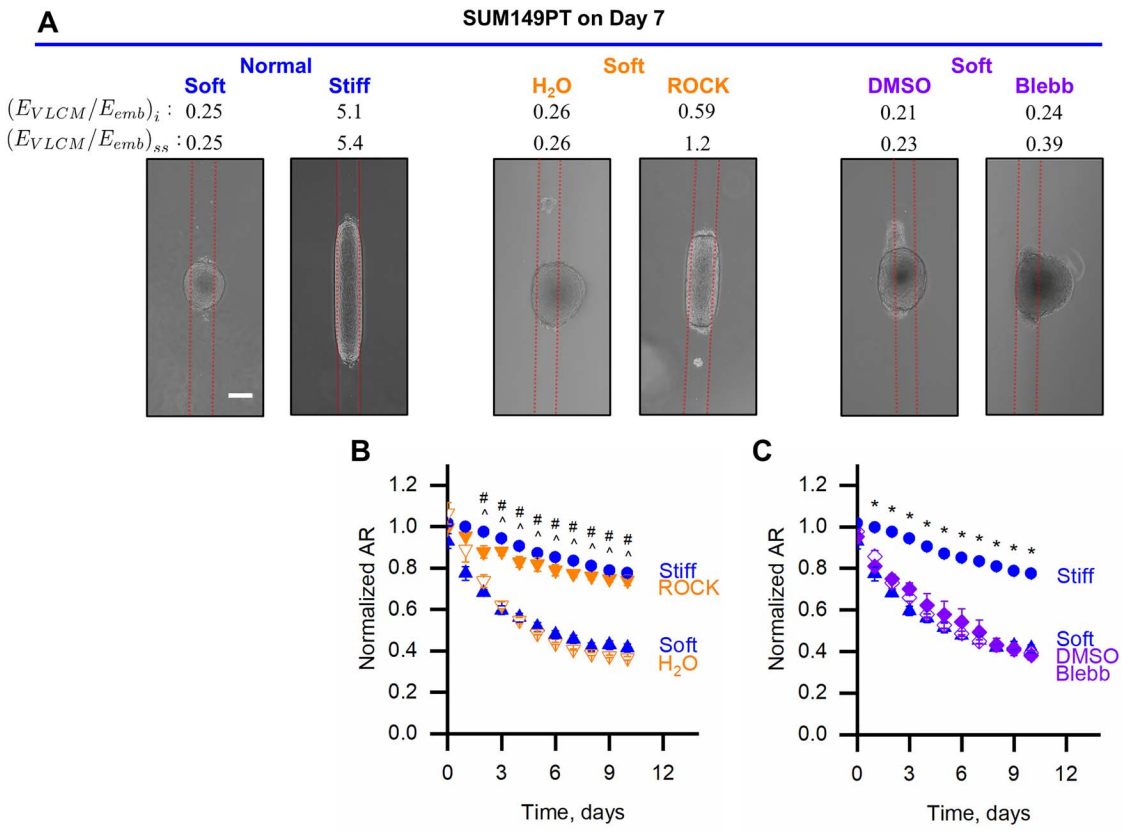

Figure 7. ROCK inhibition, but not myosin II inhibition, drives the confinement of SUM149PT emboli growth in the soft matrix VLCM. (A) Representative phase-contrast images of SUM149PT emboli grown without drug treatment (normal) or with a drug (and compared with its control) in the soft matrix VLCM. All images are taken on Day 7. Red dotted lines denote the boundaries of the VLCM. Scale bar is 200 μm. (B) Normalized aspect ratio of SUM149PT emboli treated with the ROCK inhibitor (orange triangles) compared to those grown under soft and stiff matrix VLCMs (blue triangles and circles, respectively). (C) Same as (B), but with blebbistatin (purple diamonds). Data are representative of $n \geq 3$. $*P < 0.05$ for drug treatment compared to Stiff. $^{\wedge}P < 0.05$ for drug-treatment compared to Soft. $^{\#}P < 0.05$ for drug treatment compared to control.

demonstrated a correlation between myosin-related force generation and the magnitude of the mechanical mismatch between the VLCM matrix and the tumor emboli ($E_{VLCM}/E_{emb} \neq 1$). Inhibiting myosin-related force generation generally increased the mechanical mismatch and led to different tumor growth morphologies. Here, the mechanical properties of the VLCM matrix (agarose hydrogel) in relation to those of the tumor emboli correlated with tumor emboli either elongating along the microchannel length ($E_{VLCM}/E_{emb} > 1$) or bulging into the matrix ($0 < E_{VLCM}/E_{emb} < 1$). The introduction of inhibitors that target myosin-related force generation decreased the elastic modulus and/or increased the stress relaxation of the tumor cell aggregates, effectively increasing the mechanical mismatch between the VLCM matrix and the emboli. The increased mechanical mismatch after drug treatment was correlated with increased confinement of tumor emboli growth in the soft vessel model.

Several interactions between the lymphatic vasculature and tumor cells play a role in cancer progression and metastasis [1, 17]. These include tumor lymphangiogenesis (the growth of new lymph vessels into and around a tumor) in response to growth factor signaling by tumor cells, chemokines produced by the lymphatic endothelial cells that guide tumor cells to the lymphatic vessels, lymph flow that influences how tumor cells travel or arrest within the lymphatic vessels and adhesive interactions between tumor cells and the lymphatic endothelium. All of these microenvironmental factors can influence the initiation and arrest of tumor emboli. Once a tumor embolus grows to occlude the vessel, some factors, such as lymph flow, likely will have less influence over the subsequent growth, whereas others, such as growth factors, may continue to influence emboli growth. Here, we isolated and identified important biomechanical interactions between a growing tumor embolus and the matrix surrounding a lymphatic vessel. The complexity of our model may, in the future, be increased to take into account other factors such as ECM proteins and a lymphatic endothelium.

The confinement of tumor emboli to grow within a vessel geometry—either due to an excessively stiffened matrix or weak actomyosin contractility of the tumor cells—may provide a growth advantage to the emboli. This is in contrast to what has been observed in studies of tumor spheroids fully embedded in a matrix, where solid stress has been implicated to reduce the growth of tumor spheroids by reducing proliferation and inducing apoptosis [24–26]. When confined within the stiff matrix VLCM, emboli from both cell lines ($E_{VLCM}/E_{emb} = 52$ for the HCT116 and 5.1 for the SUM149PT) grew dramatically larger in volume and without a significant reduction in growth rate, in contrast to their unconstrainted MCTS counterparts. The reasons for the dramatic growth were likely access to nutrients and space for uninhibited growth: the confinement of radial expansion imposed by the stiff matrix on emboli from both cell lines ensured that no point within the cylindrical tumor

(200 μm diameter) was >100 μm from the tumor-matrix boundary, well within the diffusion limit of oxygen in tissues (~200 μm) [80]. In addition to proximity to oxygen and nutrients, the cells had open ends into which they could expand, uninhibited. The mechanisms by which the tubular confinement increases the volumetric growth rates with respect to the unconstrained case (Supplementary Figure S5) requires further study. For example, the localization of proliferative cells in the different conditions at various time points could be determined. Recently, further insights into such experimental tumor aggregate growth in a relatively stiff (E ~ 70 kPa) alginate hydrogel tubular capsule have been provided by a mathematical model generated to reproduce the experimental behavior [31]. The experiment and model suggested that with growth along the channel, the pressure increases in the core of the tumor above a level permitting of cell proliferation, such that proliferation is likely restricted to the tips growing out along the channel [31].

Strikingly, even with an open channel into which they could expand, tumor emboli grown within the soft matrix VLCM bulged, eventually, into the matrix. Emboli morphology was correlated with the mechanical mismatch between the matrix of the VLCM and the emboli. HCT116 aggregates that were slightly more compliant than the soft VLCM matrix, $E_{VLCM}/E_{emb} = 2.6$, were initially confined to the soft matrix VLCM channel but, after 7 days, bulged into the matrix and formed oblate ellipsoids. On the other hand, SUM149PT aggregates that were much stiffer than the soft VLCM matrix, $E_{VLCM}/E_{emb} = 0.25$, maintained a spherical shape, apparently unaffected by the vessel-like constraint. This observed phenomenon has been predicted by calculations of the elastic strain energy stored in a system composed of an infinite isotropic matrix containing an inhomogeneous ellipsoidal inclusion [81]. If the inclusion is subjected to an isotropic growth strain, the elastic strain energy is minimized by a flat ellipsoidal inclusion when the inclusion is more compliant than the matrix ($E_{mat}/E_{inc} > 1$), and a sphere will minimize the elastic strain energy when the inclusion is stiffer than the matrix ($0 < E_{mat}/E_{inc} < 1$). In a previous study, we showed that tumor cell aggregates grown in agarose hydrogels display the same strain energy minimizing growth behavior as predicted by the aforementioned calculations [23].

The delayed bulging of the HCT116 tumors into the matrix of the soft matrix VLCM may be due to the development of a shell of F-actin surrounding the tumor aggregates, the thickness of which increases with the stiffness of the matrix in which the aggregate is embedded (Supplementary Figure S6) [65]. The development of the F-actin shell, suggesting a mechanosensitive response of the aggregate to confinement, has been shown to correlate with an increase the stiffness of the aggregate [65, 82]. This switch from confinement to bulging may only have been observed because the HCT116 spheroids were close in elastic modulus (117 ± 31 Pa) to the soft agarose (302 ± 11 Pa), such that the level of increase in stiffness accompanying the development of a thick F-actin shell could have inverted the mechanical mismatch. Similarly, the inability of the stiff matrix VLCM to fully constrain the tumor emboli at later time points may be attributable to the development of a thick F-actin shell and the associated actomyosin contractility. Determining the mechanisms responsible for the evolution of tumor morphology in the soft matrix VLCM presents an opportunity for further investigation.

We found that the difference in mechanical properties between the spheroids derived from the two cell lines was correlated with differential expression of myosin IIa, as seen in the western blot (Fig. 5B), and accompanying increased actomyosin contractility, as see in the contractility assays (Supplementary Figure S7). Myosin II plays a major role in the contractility of the cytoskeleton, enabling cells to generate forces for migration, remodeling and the innate stiffness of cells and tissues [71, 83–85]. Inhibition of myosin—either via ROCK (Y-27632), for which myosin II is a downstream effector, or directly (blebbistatin)—decreased the stiffness and/or increased the relaxation of tumor spheroids. The ROCK inhibitor decreased the elastic modulus of spheroids from both cell lines, which has been observed for other cells and tissues [65, 68, 86]. Blebbistatin, however, only decreased the elastic modulus of the HCT116 spheroids, not the SUM149PT spheroids. The SUM149PT cells expressed myosin II at a much higher level, which perhaps we were not able to effectively inhibit using the limited blebbistatin concentration attainable due to its poor solubility in water [79]. Notably, although the elastic modulus of the SUM149PT spheroids was not affected by blebbistatin, its relaxed, steady-state modulus was drastically affected. A large drop in the relaxed, steady-state modulus was also observed for the SUM149PT spheroids treated with the ROCK inhibitor.

Introducing the inhibitors of force generation into emboli cultures produced drastic changes in the morphology of the tumor emboli. Both inhibitors drove the HCT116 growth along the soft matrix VLCM. However, Y-27632 was less efficacious as the emboli still slightly bulged into the matrix and the normalized aspect ratio was not as large as that for emboli treated with blebbistatin, which matched that of untreated HCT116 emboli grown within the stiff matrix VLCM. Both of the inhibitor treatments reduced the elastic moduli of HCT116 spheroids to well below the soft agarose elastic (or steady-state) modulus (E_{VLCM}/E_{emb} = 6.4 for the ROCK inhibitor and 4.5 for blebbistatin). With such a significantly increased modulus mismatch between the matrix of the soft matrix VLCM and the ROCK-treated HCT116 spheroids, it is not clear why the emboli still bulged into the matrix. One possibility may be the activation of complementary pathways to ROCK, such as Rac1 and CDC42, that have the same downstream effectors, such as myosin II, enabling the HCT116 emboli to elicit force-generating activities [75, 87]. Blebbistatin, on the other hand, blocks myosin II activity regardless of the upstream activator.

The SUM149PT tumor emboli also exhibited interesting morphological responses to the drug treatments: Y-27632 was most efficacious at driving emboli growth along the channel of the soft matrix VLCM, while blebbistatin appeared to have a minimal effect. Y-27632 reduced the elastic modulus of SUM149PT spheroids, but it was still significantly greater than the elastic modulus of the soft agarose ($(E_{VLCM}/E_{emb})_i$ = 0.59, compared to 0.25 for untreated). Interestingly, because the drugs had the effect of drastically increasing the relaxation of the SUM149PT spheroids, the relaxed, steady-state modulus of the SUM149PT spheroids was just less than the steady-state modulus of the soft agarose, inverting the mechanical mismatch ($(E_{VLCM}/E_{emb})_{ss}$ = 1.2). On the other hand, blebbistatin did not affect the elastic modulus of the SUM149PT spheroids, and even taking into account the relaxation, the relaxed modulus was still significantly greater than the soft agarose ($(E_{VLCM}/E_{emb})_{ss}$ = 0.39). However, this small effect of blebbistatin did appear to allow the SUM149PT emboli in the soft matrix VLCM to initially elongate slightly along the length of the channel, which the untreated emboli did not do.

In summary, we found that the SUM149PT spheroids were ~10 times stiffer than the HCT116 spheroids, likely as a result of stronger actomyosin contractility induced by a 10-fold higher expression of myosin II, which led to an increased propensity

of the stiffer SUM149PT emboli to bulge into the matrix of the soft matrix VLCM. The higher expression of myosin II in the SUM149PT cells was also likely why blebbistatin—at the low, solubility-limited concentrations used—did not successfully allow growth of the SUM149PT emboli to be constrained by the soft matrix VLCM as it was for the blebbistatin-treated HCT116 emboli. Considerably increased relaxation of the ROCK inhibitor-treated SUM149PT spheroids, such that the mechanical mismatch with the soft agarose was shifted from less than one for the elastic moduli to greater than one for the relaxed moduli, may explain their constrained growth in the soft matrix VLCM. Finally, the prominent effect of the ROCK inhibitor on the SUM149PT emboli was not realized in the HCT116 emboli, which may be due to known cell-line dependent effects of the drug [88].

CONCLUSION

Here we demonstrated that the growth pattern of emboli correlated with the mismatch in the mechanical properties between the matrix of a VLCM and a tumor embolus. Previous studies have shown that increasing the stiffness of a full hydrogel constraint suppresses tumor growth [24, 26] and cancer cell proliferation [65]. However, in our study, increasing the constraint in the vessel-like confinement favors tumor growth. Surprisingly, we showed myosin II inhibitor-induced increases in compliance and relaxation of tumor emboli elicited confined extension of their growth in the soft matrix VLCM. Such elongation may increase tumor burden due to the increased volume of tumor within the diffusion distance of nutrients and oxygen. We modeled our channel size on lymphatic vessels, where tumor emboli are often observed; however, beyond vasculature, this cylindrical geometry also applies to the mammary duct, where the majority of mammary carcinomas initiate [89, 90]. Based on the results of this study, the effects of the cylindrical geometry of the mammary duct on the progression of mammary carcinomas may also be important to investigate.

ACKNOWLEDGEMENTS

This work was supported by the National Science Foundation [NSF CAREER 1846888 to K.L.M.] and by Rensselaer Polytechnic Institute Start-Up Funds [K.L.M.]. Likewise, we thank Elizabeth Capogna and Benjamin Liddle of Dr. Eric Ledet's lab at RPI for assistance with printing the 3D templates, Dr. Jason Herschkowitz of the University at Albany for providing the SUM149PT cell line, and the National Science Foundation [NSF MRI 1725984] for the Leica SP8 microscope.

SUPPLEMENTARY DATA

Supplementary data is available at *INTBIO* Journal online.

REFERENCES

1. Alitalo A, Detmar M. Interaction of tumor cells and lymphatic vessels in cancer progression. *Oncogene* 2012;**31**:4499–508.
2. Kerjaschki D, Bago-Horvath Z, Rudas M *et al* Lipoxygenase mediates invasion of intrametastatic lymphatic vessels and propagates lymph node metastasis of human mammary carcinoma xenografts in mouse. *J Clin Invest* 2011;**121**:2000–12.
3. Tammela T, Alitalo K. Lymphangiogenesis: molecular mechanisms and future promise. *Cell* 2010;**140**:460–76.
4. Gupta A, Deshpande CG, Badve S. Role of E-cadherins in development of lymphatic tumor emboli. *Cancer* 2003;**97**:2341–7.
5. He Y, Rajantie I, Pajusola K *et al* Vascular endothelial cell growth factor receptor 3–mediated activation of lymphatic endothelium is crucial for tumor cell entry and spread via lymphatic cessels. *Cancer Res* 2005;**65**:4739–46.
6. Massi D, Puig S, Franchi A *et al* Tumour lymphangiogenesis is a possible predictor of sentinel lymph node status in cutaneous melanoma: a case–control study. *J Clin Pathol* 2006;**59**:166.
7. Yamauchi C, Hasebe T, Iwasaki M *et al* Accurate assessment of lymph vessel tumor emboli in invasive ductal carcinoma of the breast according to tumor areas, and their prognostic significance. *Hum Pathol* 2007;**38**:247–59.
8. Moriya H, Ohbu M, Kobayashi N *et al* Lymphatic tumor emboli detected by D2-40 immunostaining can more accurately predict lymph-node metastasis. *World J Surg* 2011;**35**:2031–7.
9. Matsumoto K, Nakayama Y, Inoue Y *et al* Lymphatic microvessel density is an independent prognostic factor in colorectal cancer. *Dis Colon Rectum* 2007;**50**:308–14.
10. Pei Q, Hong Z, Tan F *et al* Intravascular emboli is an independent risk factor for the prognosis of stage III colorectal cancer patients after radical surgery. *Oncotarget* 2016;**7**:57268–76.
11. Agollah GD, Wu G, Sevick-Muraca EM *et al* In vivo lymphatic imaging of a human inflammatory breast cancer model. *J Cancer* 2014;**5**:774–83.
12. Robertson FM, Bondy M, Yang W *et al* Inflammatory breast cancer: the disease, the biology, and the treatment. *CA Cancer J Clin* 2014;**60**:351–75.
13. Tammela T, Saaristo A, Holopainen T *et al* Photodynamic ablation of lymphatic vessels and intralymphatic cancer cells prevents metastasis. *Sci Transl Med* 2011;**3**:69ra11.
14. Lauria R, Perrone F, Carlomagno C *et al* The prognostic value of lymphatic and blood vessel invasion in operable breast cancer. *Cancer* 1995;**76**:1772–8.
15. Ye Y, Tian H, Lange AR *et al* The genesis and unique properties of the lymphovascular tumor embolus are because of calpain-regulated proteolysis of E-cadherin. *Oncogene* 2013;**32**:1702–13.
16. Woodward WA, Cristofanilli M, Merajver SD *et al* Scientific summary from the Morgan Welch MD Anderson cancer center inflammatory breast cancer (IBC) program 10th anniversary conference. *J Cancer* 2017;**8**:3607–14.
17. Podgrabinska S, Skobe M. Role of lymphatic vasculature in regional and distant metastases. *Microvasc Res* 2014;**95**:46–52.
18. Lehman HL, Dashner EJ, Lucey M *et al* Modeling and characterization of inflammatory breast cancer emboli grown in vitro. *Int J Cancer* 2013;**132**:2283–94.
19. Theodoraki MA, Rezende CO Jr, Chantarasriwong O *et al* Spontaneously-forming spheroids as an in vitro cancer cell model for anticancer drug screening. *Oncotarget* 2015;**6**:21255–67.
20. Fong ELS, Harrington DA, Farach-Carson MC *et al* Heralding a new paradigm in 3D tumor modeling. *Biomaterials* 2016;**108**:197–213.
21. Unger C, Kramer N, Walzl A *et al* Modeling human carcinomas: physiologically relevant 3D models to improve anticancer drug development. *Adv Drug Deliv Rev* 2014;**79**:50–67.
22. Zanoni M, Piccinini F, Arienti C *et al* 3D tumor spheroid models for in vitro therapeutic screening: a systematic approach

to enhance the biological relevance of data obtained. *Sci Rep* 2016;**6**:1–11.
23. Mills KL, Kemkemer R, Rudraraju S *et al* Elastic free energy drives the shape of prevascular solid tumors. *PLoS One* 2014;**9**:e103245.
24. Helmlinger G, Netti PA, Lichtenbeld HC *et al* Solid stress inhibits the growth of multicellular tumor spheroids. *Nature* 1997;**15**:778–83.
25. Cheng G, Tse J, Jain RK *et al* Micro-environmental mechanical stress controls tumor spheroid size and morphology by suppressing proliferation and inducing apoptosis in cancer cells. *PLoS One* 2009;**4**:e4632.
26. Delarue M, Montel F, Vignjevic D *et al* Compressive stress inhibits proliferation in tumor spheroids through a volume limitation. *Biophys J* 2014;**107**:1821–8.
27. He L, Chen W, Wu P-H *et al* Local 3D matrix confinement determines division axis through cell shape. *Oncotarget* 2015;**7**:6994–7011.
28. Nam S, Chaudhuri O. Mitotic cells generate protrusive extracellular forces to divide in three-dimensional microenvironments. *Nat Phys* 2018;**14**:621–8.
29. Tse JM, Cheng G, Tyrrell JA *et al* Mechanical compression drives cancer cells toward invasive phenotype. *Proc Natl Acad Sci USA* 2012;**109**:911–6.
30. Northcott JM, Dean IS, Mouw JK *et al* Feeling stress: the mechanics of cancer progression and aggression. *Front Cell Dev Biol* 2018;**6**:17.
31. Le Maout V, Alessandri K, Gurchenkov B *et al* Role of mechanical cues and hypoxia on the growth of tumor cells in strong and weak confinement: a dual in vitro–in silico approach. *Sci Adv* 2020;**6**:eaaz7130.
32. van Deurzen CHM, Borgstein PJ, van Diest PJ. In-transit lymph node metastases in breast cancer: a possible source of local recurrence after sentinel node procedure. *J Clin Pathol* 2008;**61**:1314–6.
33. van Uden DJP, van Laarhoven HWM, Westenberg AH *et al* Inflammatory breast cancer: an overview. *Crit Rev Oncol Hematol* 2015;**93**:116–26.
34. Rubiano A, Delitto D, Han S *et al* Viscoelastic properties of human pancreatic tumors and in vitro constructs to mimic mechanical properties. *Acta Biomater* 2018;**67**:331–40.
35. Stewart DC, Rubiano A, Dyson K *et al* Mechanical characterization of human brain tumors from patients and comparison to potential surgical phantoms. *PLoS One* 2017;**12**:1–19.
36. Nam S, Gupta VK, Lee HP *et al* Cell cycle progression in confining microenvironments is regulated by a growth-responsive TRPV4-PI3K/Akt-p27Kip1 signaling axis. *Sci Adv* 2019;**5**:eaaw6171.
37. Brock LM. Rapid indentation of a pre-stressed hyper-elastic half-space: comparison of axially symmetric and plane strain cases. *Int J Solids Struct* 2001;**38**:5527–43.
38. Zuidema JM, Rivet CJ, Gilbert RJ *et al* A protocol for rheological characterization of hydrogels for tissue engineering strategies. *J Biomed Mater Res, Part B Appl Biomater* 2014;**102**:1063–73.
39. Hogrebe NJ, Reinhardt JW, Gooch KJ. Biomaterial microarchitecture: a potent regulator of individual cell behavior and multicellular organization. *J Biomed Mater Res, Part A* 2016;**105**:640–61.
40. Chaudhuri O, Gu L, Klumpers D *et al* Hydrogels with tunable stress relaxation regulate stem cell fate and activity. *Nat Mater* 2016;**15**:326–34.
41. Marmottant P, Mgharbel A, Käfer J *et al* The role of fluctuations and stress on the effective viscosity of cell aggregates. *Proc Natl Acad Sci USA* 2009;**106**:17271–5.
42. Giverso C, Stefano SD, Grillo A *et al* A three dimensional model of multicellular aggregate compression. *Soft Matter* 2019;**15**:10005–19.
43. Foty RA, Steinberg MS. The differential adhesion hypothesis: a direct evaluation. *Dev Biol* 2005;**278**:255–63.
44. Guevorkian K, Colbert M-J, Durth M *et al* Aspiration of biological viscoelastic drops. *Phys Rev Lett* 2010;**104**:218101.
45. Preziosi L, Ambrosi D, Verdier C. An elasto-visco-plastic model of cell aggregates. *J Theor Biol* 2010;**262**:35–47.
46. Gong X, Kulwatno J, Mills KL. Rapid fabrication of collagen bundles mimicking tumor-associated collagen architectures. *Acta Biomater* 2020;**108**:128–41.
47. Carpenter AE, Jones TR, Lamprecht MR *et al* CellProfiler: image analysis software for identifying and quantifying cell phenotypes. *Genome Biol* 2006;**7**:R100.
48. Roudsari LC, West JL. Studying the influence of angiogenesis in in vitro cancer model systems. *Adv Drug Deliv Rev* 2016;**97**:250–9.
49. Carmeliet P, Jain RK. Angiogenesis in cancer and other diseases. *Nature* 2000;**407**:249–57.
50. Margaris KN, Black RA. Modelling the lymphatic system: challenges and opportunities. *J R Soc Interface* 2012;**9**:601–12.
51. Platt AM, Randolph GJ. Dendritic cell migration through the lymphatic vasculature to lymph nodes. In: *Advances in Immunology*. Amsterdam, Elsevier Inc., 2013, 51–68.
52. Ulrich TA, Jain A, Tanner K *et al* Probing cellular mechanobiology in three-dimensional culture with collagen-agarose matrices. *Biomaterials* 2010;**31**:1875–84.
53. Brauchle E, Kasper J, Daum R *et al* Biomechanical and biomolecular characterization of extracellular matrix structures in human colon carcinomas. *Matrix Biol* 2018;**68**:180–93.
54. Stewart DC, Berrie D, Li J *et al* Quantitative assessment of intestinal stiffness and associations with fibrosis in human inflammatory bowel disease. *PLoS One* 2018;**13**:e0200377.
55. Plodinec M, Loparic M, Monnier CA *et al* The nanomechanical signature of breast cancer. *Nat Nanotechnol* 2012;**7**:757–65.
56. Samani A, Bishop J, Luginbuhl C *et al* Measuring the elastic modulus of ex vivo small tissue samples. *Phys Med Biol* 2003;**48**:2183–98.
57. Matsumura T, Umemoto T, Fujihara Y, *et al* Measurement of elastic property of breast tissue for elasticity imaging. *IEEE International Ultrasonics Symposium Proceedings*. 2009. 1451–1454.
58. Ivascu A, Kubbies M. Rapid generation of single-tumor spheroids for high-throughput cell function and toxicity analysis. *J Biomol Screen* 2006;**11**:922–32.
59. Kelm JM, Timmins NE, Brown CJ *et al* Method for generation of homogeneous multicellular tumor spheroids applicable to a wide variety of cell types. *Biotechnol Bioeng* 2003;**83**:173–80.
60. Lin R-Z, Chang H-Y. Recent advances in three-dimensional multicellular spheroid culture for biomedical research. *Biotechnol J* 2008;**3**:1172–84.
61. Mueller-Klieser WF, Sutherland RM. Oxygen consumption and oxygen diffusion properties of multicellular spheroids from two different cell lines. In: Bruley D, Bicher HI, Reneau D (eds.). *Oxygen Transport to Tissue—VI*. Boston, MA, Springer US, 1984, 311–21.

62. Alessandri K, Ranjan B, Valérïévitch V *et al* Cellular capsules as a tool for multicellular spheroid production and for investigating the mechanics of tumor progression in vitro. *Proc Natl Acad Sci* 2013;**110**:14843–8.
63. Drasdo D, Höhme S. A single-cell-based model of tumor growth in vitro: monolayers and spheroids. *Phys Biol* 2005;**2**:133–47.
64. Butcher DT, Alliston T, Weaver VM. A tense situation: forcing tumour progression. *Nat Rev Cancer* 2009;**9**:108–22.
65. Taubenberger AV, Girardo S, Träber N *et al* 3D microenvironment stiffness regulates tumor spheroid growth and mechanics via p21 and ROCK. *Adv Biosyst* 2019;**3**: 1900128.
66. Tavares S, Vieira AF, Taubenberger AV *et al* Actin stress fiber organization promotes cell stiffening and proliferation of pre-invasive breast cancer cells. *Nat Commun* 2017;**8**: 15237.
67. Barriga EH, Franze K, Charras G *et al* Tissue stiffening coordinates morphogenesis by triggering collective cell migration in vivo. *Nature* 2018;**554**:523–7.
68. Gullekson C, Cojoc G, Schürmann M *et al* Mechanical mismatch between Ras transformed and untransformed epithelial cells. *Soft Matter* 2017;**13**:8483–91.
69. Paszek MJ, Zahir N, Johnson KR *et al* Tensional homeostasis and the malignant phenotype. *Cancer Cell* 2005;**8**:241–54.
70. Levental KR, Yu H, Kass L *et al* Matrix crosslinking forces tumor progression by enhancing integrin signaling. *Cell* 2009;**139**:891–906.
71. Samuel MS, Lopez JI, McGhee EJ *et al* Actomyosin-mediated cellular tension drives increased tissue stiffness and β-catenin activation to induce epidermal hyperplasia and tumor growth. *Cancer Cell* 2011;**19**:776–91.
72. Nederman T, Norling B, Glimelius B *et al* Demonstration of an extracellular matrix in multicellular tumor. *Cancer Res* 1984;**44**:3090–7.
73. Lee W, Kalashnikov N, Mok S *et al* Dispersible hydrogel force sensors reveal patterns of solid mechanical stress in multicellular spheroid cultures. *Nat Commun* 2019;**10**:1–14.
74. Amin E, Dubey BN, Zhang SC *et al* Rho-kinase: regulation, (dys)function, and inhibition. *Biol Chem* 2013;**394**:1399–410.
75. Prudnikova TY, Rawat SJ, Chernoff J. Molecular pathways: targeting the kinase effectors of RHO-family GTPases. *Clin Cancer Res* 2015;**21**:24–9.
76. Pandya P, Orgaz JL, Sanz-Moreno V. Modes of invasion during tumour dissemination. *Mol Oncol* 2017;**11**:5–27.
77. Shutova M, Yang C, Vasiliev JM *et al* Functions of nonmuscle myosin II in assembly of the cellular contractile system. *PLoS One* 2012;**7**:e40814.
78. Chan CJ, Ekpenyong AE, Golfier S *et al* Myosin II activity softens cells in suspension. *Biophys J* 2015;**108**:1856–69.
79. Rauscher A, Gyimesi M, Kovács M *et al* Targeting myosin by blebbistatin derivatives: optimization and pharmacological potential. *Trends Biochem Sci* 2018;**43**:700–13.
80. Wilson WR, Hay MP. Targeting hypoxia in cancer therapy. *Nat Rev Cancer* 2011;**11**:393–410.
81. Mura T. Ellipsoidal inhomogeneities. In: *Micromechanics of Defects In Solids*. Dordrecht, Netherlands, Springer, 1987, 177–239.
82. Fischer-Friedrich E. Active prestress leads to an apparent stiffening of cells through geometrical effects. *Biophys J* 2018;**114**:419–24.
83. Zhou J, Kim HY, Davidson LA. Actomyosin stiffens the vertebrate embryo during crucial stages of elongation and neural tube closure. *Development* 2009;**136**:677–88.
84. Lecuit T, Lenne PF. Cell surface mechanics and the control of cell shape, tissue patterns and morphogenesis. *Nat Rev Mol Cell Biol* 2007;**8**:633–44.
85. Paul CD, Mistriotis P, Konstantopoulos K. Cancer cell motility: lessons from migration in confined spaces. *Nat Rev Cancer* 2017;**17**:131–40.
86. Srinivasan S, Ashok V, Mohanty S *et al* Blockade of rho-associated protein kinase (ROCK) inhibits the contractility and invasion potential of cancer stem like cells. *Oncotarget* 2017;**8**:21418–28.
87. Arias-Romero LE, Chernoff J. Targeting CDC42 in cancer. *Expert Opin Ther Targets* 2013;**17**:1263–73.
88. Wei L, Surma M, Shi S *et al* Novel insights into the roles of rho kinase in cancer. *Arch Immunol Ther Exp (Warsz)* 2016;**64**:259–78.
89. Brock EJ, Ji K, Shah S *et al* In vitro models for studying invasive transitions of ductal carcinoma in situ. *J Mammary Gland Biol Neoplasia* 2019;**24**:1–15.
90. Nelson AC, Machado HL, Schwertfeger KL. Breaking through to the other side: microenvironment contributions to DCIS initiation and progression. *J Mammary Gland Biol Neoplasia* 2018;**23**:207–21.